



Detailed impedance characterization of a well performing and durable Ni:CGO infiltrated cermet anode for metal-supported solid oxide fuel cells

Jimmi Nielsen*, Trine Klemensø, Peter Blennow

Department of Energy Conversion and Storage, Technical University of Denmark – DTU, Frederiksborgvej 399, DK-4000 Roskilde, Denmark

HIGHLIGHTS

- ▶ Impedance of the infiltrated cermet anode was described by Porous Electrode Theory.
- ▶ The characteristic electrochemical utilization thickness was estimated.
- ▶ CGO self-limiting growth and Ni fixation in CGO matrix stabilize the infiltration.
- ▶ The impact of corrosion on the impedance was studied.

ARTICLE INFO

Article history:

Received 25 April 2012

Received in revised form

28 June 2012

Accepted 13 July 2012

Available online 20 July 2012

Keywords:

Impedance spectroscopy

Porous electrode theory

Infiltration

Anode

Metal support

Solid oxide fuel cell

ABSTRACT

Further knowledge of the novel, well performing and durable Ni:CGO infiltrated cermet anode for metal supported fuel cells has been acquired by means of a detailed impedance spectroscopy study. The anode impedance was shown to consist of three arcs. Porous electrode theory (PET) represented as a transmission line response could account for the intermediate frequency arc. The PET model enabled a detailed insight into the effect of adding minor amounts of Ni into the infiltrated CGO and allowed an estimation of important characteristics such as the electrochemical utilization thickness of the anode. Furthermore, the study also revealed that the observed high frequency impedance arc cannot solely be a consequence of the grain boundaries within the electrolyte as previous studies have assumed. Instead, the results pointed towards an oxide ion charge transfer resistance between the electrolyte and the infiltrated anode. The low frequency impedance arc was in accordance with previous studies interpreted to be associated with the gas concentration. Finally, the robustness of the infiltration towards sintering and/or agglomeration at elevated temperature was studied. The results showed that the performance of the infiltrated submicron sized particles was surprisingly robust. TEM analysis revealed the nano sized Ni particles to be trapped within the CGO matrix, which along the self limiting grain growth of the CGO seem to be able to stabilize the submicron structured anode.

© 2012 Elsevier B.V. All rights reserved.

1. Introduction

Solid oxide fuel cells (SOFCs) offer the possibility of power generation with a higher efficiency than conventional combustion systems. However, in terms of cost and durability SOFCs are not yet competitive. The last decades of SOFC research has mainly focused on going towards lower operating temperature. It is generally believed that this has several advantages such as increased durability and the possibility of a wider choice of materials, which increases the chances for the SOFC technology to lower cost and to become sufficiently competitive. Metal supported SOFCs are in this

context promising. Besides lower material cost with the potential use of commercial available stainless steel, metal supported cells (MSC) has some advantages compared to the traditional high (1000–750 °C) and intermediate (750–650 °C) temperature purely ceramic based SOFCs. These advantages are among other things higher thermal conductivity and ductility of the support, which in particular is an advantage in small-scale and mobile systems where tolerance towards e.g. the presence of shock vibrations, thermal cycling, electrical load transients, and redox cycles may be important [1–3].

The introduction of metal into SOFCs raises some new challenges with respect to cell fabrication, since the usual sintering in an oxidizing atmosphere of the various components such as the electrolyte (above 1200 °C) and the cathode (above 1000 °C) used for conventional ceramic based SOFC fabrication needs to be

* Corresponding author. Tel.: +45 46775626.

E-mail address: jini@dtu.dk (J. Nielsen).

avoided [3,4]. Further, the combination of the traditional Ni-YSZ anode and FeCr stainless steel at high temperatures may lead to the formation of Ni–Cr–Fe alloys or insulating oxides in the anode layer, which are detrimental to cell performance and durability [2,5]. The MSC design developed at DTU Energy Conversion (former Risø DTU) involves a novel anode, substituting the conventional SOFC Ni/YSZ cermet anode. The novel anode consists of a stainless steel based cermet backbone, which as a final step in the cell fabrication is infiltrated with Ni:CGO. MSC's with this type of anode have been demonstrated on single cell level (active area 16 cm^2) to show excellent performance and durability with a degradation rate of 0.9% pr. 1000 h during in total 3000 h of 0.25 A cm^{-2} galvanostatic testing at 650°C [4]. Further, it was also shown on button cells (active area of 0.5 cm^2) that with the combination of a dense CGO barrier layer and an LSC cathode a performance with an area specific resistance (ASR) of $0.27 \Omega\text{cm}^2$ at 650°C could be obtained. These performance and durability characteristics are very encouraging and despite several papers on metal supported SOFC with this type of infiltrated anode [3,4,6,7], the impedance and the factors controlling the performance and durability of this type of anode is at this point not well understood. Some preliminary impedance data on symmetrical cells with the Ni:CGO infiltrated stainless steel based cermet anode backbone with respect to temperature and gas concentration dependency has nonetheless been reported [3,6].

In the present paper we report the first detailed impedance characterization of the cermet based anode with Ni:CGO infiltration by e.g. studying the influence on the impedance of Ni content, the amount of infiltration, backbone composition, impedance development during initial startup and the effect of temperature and thus sintering of the infiltrated Ni:CGO. The direct infiltration on a stainless steel based cermet backbone must necessarily lead to an interaction between the infiltrated Ni:CGO and the stainless steel surface, which consist of a chromium oxide scale that protects the stainless steel bulk against corrosion. The interaction and impact of corrosion of the metal backbone on the impedance is studied by a stepwise increase in steam content and an accelerated corrosion test at 750°C . The aspect of corrosion is of high importance since the MSC's needs to be able to withstand the technological relevant condition of high fuel utilization without severe detrimental corrosion.

2. Experimental

2.1. Symmetrical cell preparation

The ferritic stainless steel metal powders (22% Cr-based stainless steel alloy) used in the preparation of the symmetrical cells were selected based on particle size distributions suitable for tape casting. The organic solvent-based slurries contained (in addition to the metal powder) polymeric binder, plasticizer, and other organic additives necessary for the fabrication process. For fabrication of the cermet (ceramic + metal) anode layer used as backbone in the symmetrical cells, tape casting slurries were prepared

composed of ZrO_2 co-doped with Sc_2O_3 and Y_2O_3 (hereafter referred to as ScYSZ). After drying, the multi-layer cells were formed by bonding of the individual tapes together by lamination (application of temperature and pressure). Subsequently, the resulting multilayered tapes were heat treated in air for debinding, followed by co-sintering under proprietary conditions in a low oxygen partial pressure $p(\text{O}_2)$ atmosphere (H_2/Ar). After co-sintering, the electro catalytically active phase was infiltrated into the porous structure to generate the fuel electrode. For the infiltration, aqueous precursor solutions of various nitrate salts (Alfa Aesar) were prepared by mixing stoichiometric and calibrated amounts of precursors together with a suitable surfactant. After infiltration, the cells were calcined at 350°C in air for 2 h. The amount (wt.%) of infiltrated material in the porous electrodes was estimated by weighing the cells before and after infiltration and calcination and subtracting the approximate weight of the electrolyte. The infiltration procedure ensured a uniform coating of submicron-sized particles on all the surfaces of the porous structure. Further details on the cell fabrication can be found in the patent literature [8].

2.2. Electrochemical characterization

All the measurements on symmetrical cells with 50 vol % 3YSZ in the cermet backbone are throughout the paper referred to as normal backbone composition. The $6 \times 6 \text{ mm}$ symmetrical cells with the normal backbone composition were all cut out from the same laminated symmetrical cell making the measurements highly comparable. Pt-paste was applied onto the electrodes to form a current collection layer. The cells were characterized by electrochemical impedance spectroscopy (EIS) at open circuit voltage (OCV) at different temperatures $650\text{--}800^\circ\text{C}$ and hydrogen/water gas mixtures. All symmetrical cell measurements were, unless otherwise stated, conducted with an initial ramping to 800°C followed by a stepwise ramping down to 650°C . During the ramping from 800°C to 650°C EIS spectra were recording at selected temperatures. The measurements were conducted in specially designed rigs, which have been constructed to allow for simultaneous testing of four symmetric cells per test run, with fully automated changes of testing conditions, such as temperature, and gas composition. Further details on the electrochemical setup can be found elsewhere [9].

The EIS spectra were obtained with a Solartron 1260 FRA using a 25 mV amplitude. The impedance data were analyzed in a MatLab laboratory developed program with equivalent circuit model fitting with the use of the complex non-linear least square (CNLS) fitting routine. For visualization at which frequencies two impedance spectra differ from each other, the method Analysis of Difference in Impedance Spectra (ADIS) was employed [10,11]. In the ADIS method the difference between the derivative of the real part of the impedance $\Delta(\partial Z'/\partial \ln(f))$ is plotted as a function of $\log(\text{frequency})$. Since $Z'(f)$ is only known for a discrete set of frequencies $\{f_1, f_2, \dots, f_N\}$, $\Delta(\partial Z'/\partial \ln(f))$ may for the n th frequency between 2 and $N - 1$ be written as [11]:

$$\Delta Z'(f_n) = \Delta \left(\frac{\partial Z'}{\partial \ln(f_n)} \right) \cong \frac{[Z'_B(f_{n+1}) - Z'_B(f_{n-1})] - [Z'_A(f_{n+1}) - Z'_A(f_{n-1})]}{\ln(f_{n+1}) - \ln(f_{n-1})} \quad (1)$$

with 30–50 vol.% 3% Y_2O_3 -doped ZrO_2 (3YSZ). A similar processing technique was used to fabricate the approximately $120 \mu\text{m}$ thick electrolyte tape for the symmetrical cells. The electrolyte was

The ADIS method can without any preceding assumptions help to visualize at which frequencies the impedance spectra are affected by a change. From knowing the frequency domains of the

individual cell processes in the overall impedance spectrum of a fuel cell, it may be possible from changes in a given frequency domain to pinpoint which process or processes that degrade or activate during operation. The used notation for equivalent circuits is that of Bernard Boukamp [12].

2.3. Microstructural characterization

The microstructure of the samples, both before and after electrochemical characterization, was investigated by inspection of polished cross-sections in a Zeiss Supra 25 scanning electron microscope (SEM) equipped with an energy dispersive X-ray spectrometry system (EDS) and with a Hitachi TM1000 tabletop SEM. The polished cross-sections were prepared by vacuum embedding the samples in Struers epoxy resin (Epofix); ground using SiC paper; polished using 6, 3 and 1 μm diamond paste, and then carbon coated to eliminate surface charging.

A TEM sample was prepared using the focused ion beam (FIB) on a Zeiss Crossbeam 1540XB equipped with a field emission gun. The FIB was operated at 30 keV during milling. For TEM investigation, a JEOL 3000F TEM/STEM (Tokyo, Japan) operated at 300 keV equipped with a field-emission gun and an EDS system was used.

An Oxford Instruments INCA system (Abingdon, United Kingdom) was used for collecting EDS spectra.

3. Results and discussion

3.1. Deconvolution of the infiltrated cermet anode impedance

Figs. 1 and 2 show impedance spectra at various temperatures for anode cermets infiltrated with respectively $\text{Ce}_{0.8}\text{Gd}_{0.2}\text{O}_{1.9}$ (CGO) and a mixture of 10 wt% Ni in CGO (Ni:CGO). The cermet backbone consists of ferritic stainless steel FeCr and 3% yttria stabilized zirconia (3YSZ) as described in the experimental section 2.1. A previous report on the characterization of the Ni:CGO infiltrated anode identified three impedance arcs in the impedance spectra [6], which is in qualitative accordance with the spectra in Fig. 2. In the previous study, the high frequency (HF) arc was ascribed the grain boundaries of the electrolyte, the intermediate frequency arc was ascribed the electrochemistry of the electrode reaction, while the low frequency arc was shown to be related to the gas composition. That is, the resistance associated with the coupled gas diffusion in the porous anode and gas conversion. The general term gas concentration impedance is used for these effects associated

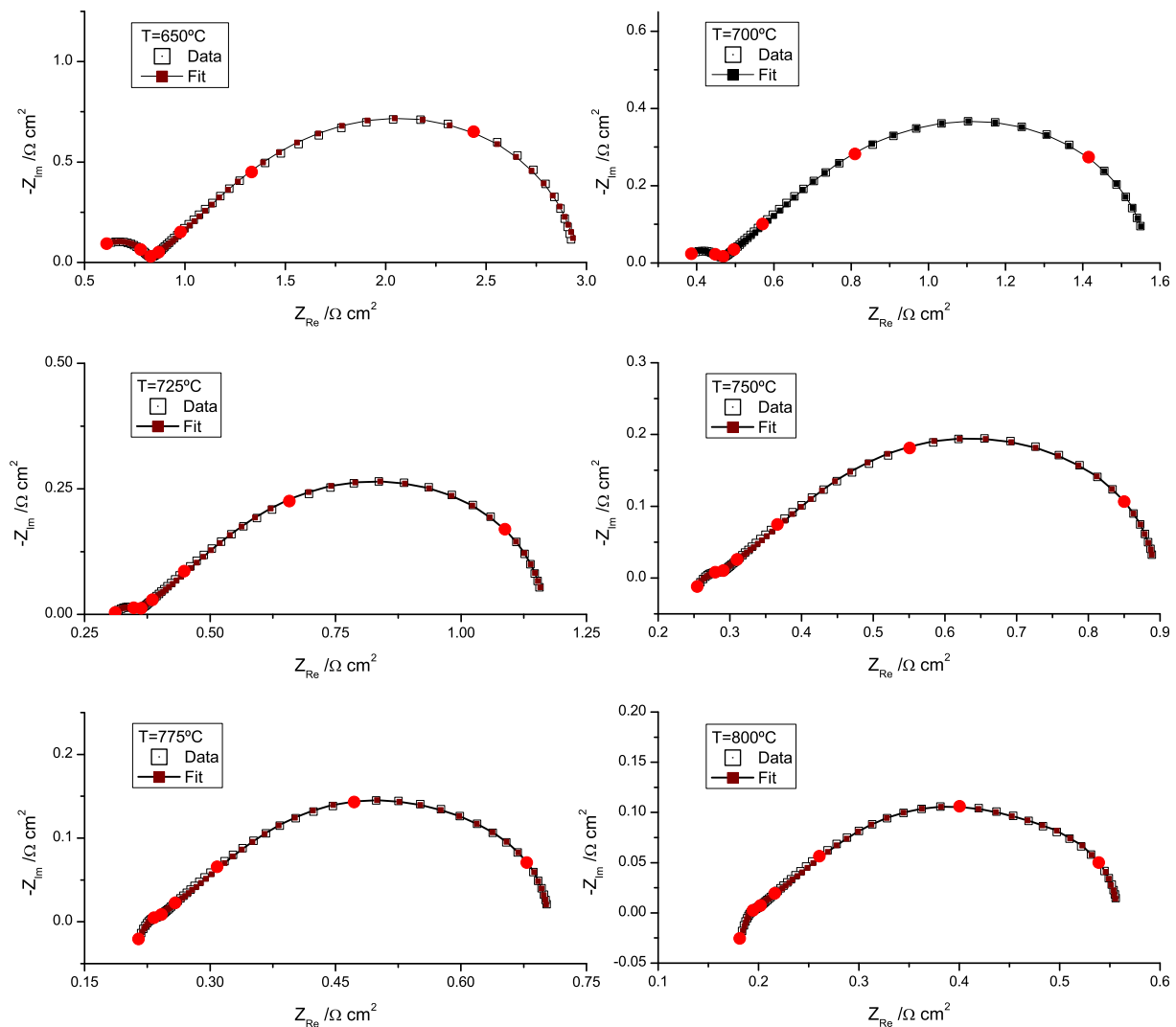


Fig. 1. Measured and fitted impedance spectra of a symmetrical cell with a CGO infiltrated cermet anode in the temperature range 650–800 °C. All measurements were in a 3% humidified hydrogen atmosphere. The red dots ● denote each frequency decade in the frequency range 1 MHz–1 Hz. The fits have been done with the equivalent circuit $L(R_{HF} Q_{HF}) PET(R_{Conv}, C_{Conv})$. (For interpretation of the references to color in this figure legend, the reader is referred to the web version of this article.)

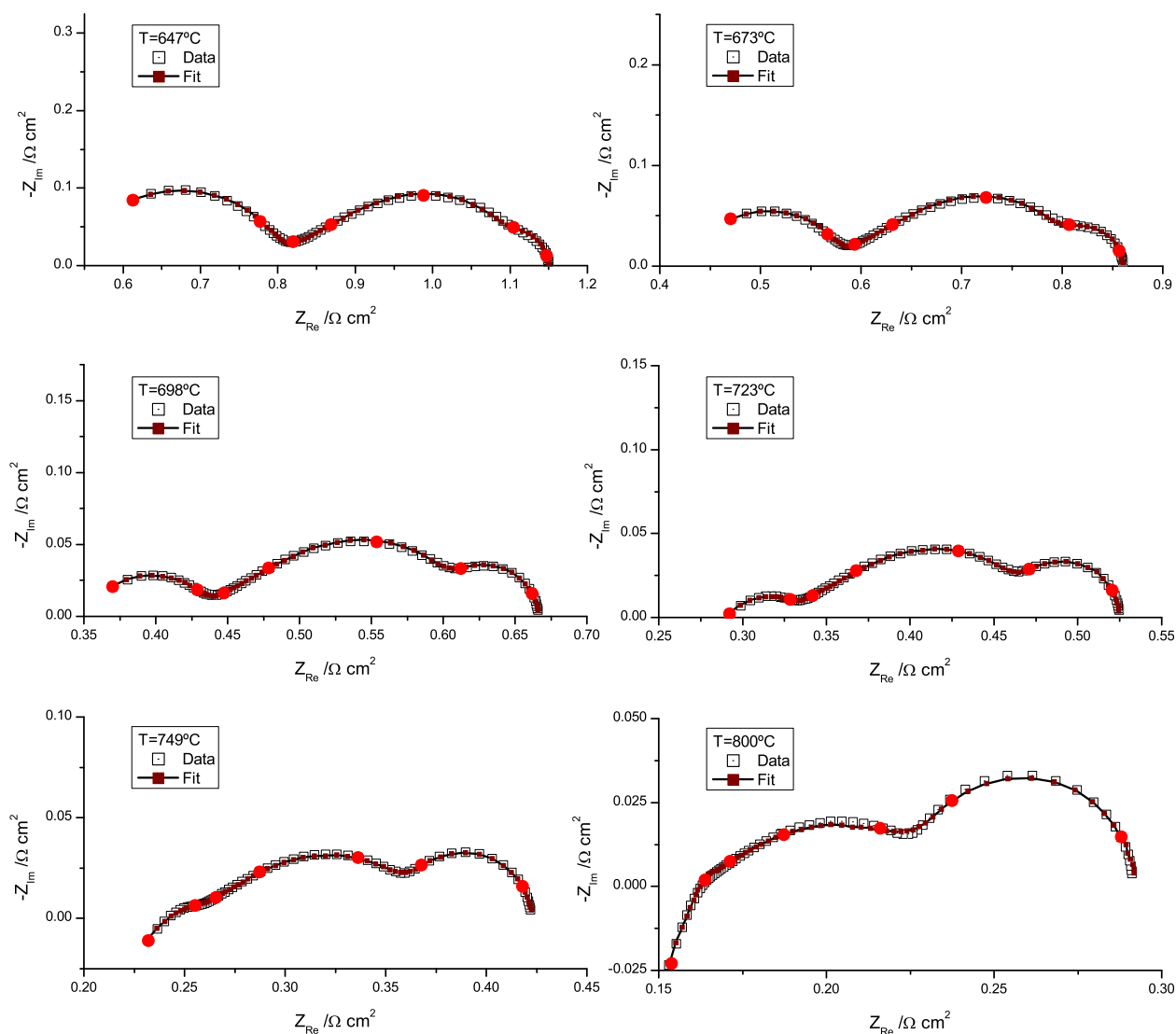


Fig. 2. Measured and fitted impedance spectra of a symmetrical cell with a Ni:CGO infiltrated cermet anode in the temperature range 650–800 °C. All measurements were in a 3% humidified hydrogen atmosphere. The red dots ● denote each frequency decade in the frequency range 1 MHz–1 Hz. The fits have been done with the equivalent circuit $L(R_{HF} Q_{HF})PET(R_{Conv}, C_{Conv})$. (For interpretation of the references to color in this figure legend, the reader is referred to the web version of this article.)

with the gas transport of reactants to and reaction products from the electrochemical active part of the electrode. The effects will always be present and can be observed by impedance spectroscopy if the resistance of the electrochemical reaction is sufficiently small as in the cases shown in Fig. 2. Various aspects of the impedance of the mentioned gas transport phenomena have been studied in detail by numerical calculations [13–15] and through analytical solutions [16,17]. From these studies it was shown that the impedance of the coupled gas diffusion and gas conversion in general has the shape of a Finite-Length-Warburg (FLW) type diffusion impedance at high frequencies and the shape of a semicircle at low frequencies. In the limiting case, where the resistance associated with diffusion is dominating a Finite-Length-Warburg (FLW) type diffusion impedance is observed. In the opposite case, where the resistance associated with gas conversion is dominating the impedance response can, to a good approximation, be modeled as a semicircle meaning a parallel combination of a resistor and a capacitor. In the intermediate situation, an approximation has sometimes been made by modeling the coupled gas diffusion and gas conversion impedance as two semicircles in series [9,18]. For

the condition of 3% humidified hydrogen atmosphere at OCV, the setup as in the studies [6,9,17], and the similar conditions of the present results in Figs. 1 and 2, the coupled gas diffusion and gas conversion is as a good approximation and for simplicity modeled as a parallel combination between a resistor R_{Conv} and a capacitor C_{Conv} . Fitting of the low frequency arc with a semicircle and a Finite-Length-Warburg impedance response has both been attempted in the fitted spectra of Figs. 1 and 2. It was found that a semicircle gave the best and most stable fits. Thus, the resistance from the gas diffusion within the porous electrode structure is neglected.

An examination of the spectra in Figs. 1 and 2 shows that the intermediate frequency arc associated with the electrochemistry is significantly larger in the case of CGO infiltration than in the case with Ni:CGO infiltration. Hence, the addition of minor amounts of Ni improves the performance of the anode considerably as already reported in Ref. [6]. Further, from the spectra of the anode with CGO infiltration it is possible to see that the shape of the impedance arc associated with the electrochemistry cannot be described by a suppressed semicircle as done in Ref. [6]. The same conclusions can be made regarding the shape of the intermediate frequency arc

in the spectra with Ni:CGO infiltration in Fig. 2, but not as convincingly due to the overlap from the other impedance arcs. The clearly observed skewed semicircle shape of the impedance is characteristic for a porous electrode consisting of both ionically and electronically connected networks. This type of porous electrode is widely used since it increases the effective active area of the electrode considerably. The coupling between the transports of ionic species through an ionic pathway in the porous electrode with an electrochemical reaction taking place along the ionic pathway is the origin to the observed impedance spectrum shape of a skewed semicircle. The porous structure of the electrode can be modeled as columns coated by an infiltrated CGO-based layer and described by the general transmission line presented in Fig. 3. Here χ_1 and χ_2 represents the impedance pr. unit length ($\Omega \text{ m}^{-1}$) of the ionic and the electronic rail, while ζ is an impedance-length ($\Omega \text{ m}$) representing the electrode/gas interfacial impedance. The unit of ζ is $\Omega \text{ m}$ since it is the area specific impedance of the surface reaction ($\Omega \text{ m}^2$) divided by the perimeter of the column (metal + infiltration).

The impedance of the above described coupling in Fig. 3 has been explored for porous electronic conducting electrodes in aqueous electrolyte solutions, where an analytical solution for the impedance was developed by de Levie [19]. In this context the porous structure filled with an aqueous electrolyte was modeled as cylindrical pores in an electronic conducting solid electrode. The situation can be described by the same transmission line as depicted in Fig. 3. It was assumed that the impedance of the electronic rail χ_2 is negligible compared to the impedance of the ionic rail χ_1 . Since then, various aspects of the solution have been studied and reported in the literature, which recently has been reviewed by Andrej Lasia [20]. Despite that the main development and application of this porous electrode theory is associated with electrodes in an aqueous solution, the theory is also applicable for solid state systems. The theory has e.g. recently been used to account for the impedance of the conventional Ni:YSZ cermet SOFC anode [21]. Furthermore, the ionic and electronic rail in the transmission line of Fig. 3 can also be represented by the same material as in the case of mixed ionic electronic conducting (MIEC) material based cathodes for intermediate temperature SOFC (IT-SOFC). In this case the ionic transport mechanism is solid state diffusion of oxide ions and the impedance

describing the co-limiting situation of a coupling between diffusion and a reaction is usually referred to as Gerischer impedance [22,23]. Thus, the distributed impedance presented by the transmission line in Fig. 3 is representative for many types of different porous electrodes. The difference in the application of the transmission line lies in the physical interpretation of the involved impedance elements.

The following general solution for the transmission line shown in Fig. 3 has been developed in Refs. [24,25]:

$$Z = \frac{\chi_1 \chi_2}{\chi_1 + \chi_2} \left(l + \frac{2\lambda}{\sinh(l/\lambda)} \right) + \lambda \frac{\chi_1^2 + \chi_2^2}{\chi_1 + \chi_2} \coth\left(\frac{l}{\lambda}\right) \quad (2)$$

with

$$\lambda = \sqrt{\frac{\zeta}{\chi_1 + \chi_2}} \quad (3)$$

Here l is the thickness of the electrode and λ is the characteristic AC penetration length or equivalent the electrochemical utilization thickness of the electrode. Eq. (2) represents the impedance of a single column (Ω) shown in Fig. 3, but in principle the porous electrode consists of n columns pr. area. However, it is difficult to determine the exact number of columns pr. area in the porous electrode. A much easier and equivalently informative approach is to consider the porous electrode effectively as one column pr. area. This enables a direct application of Eq. (2). Since the electronic rail in the present case is represented by the electronically well conducting stainless steel backbone the condition $\chi_2 \ll \chi_1$ is valid, which results in Eq. (2) being simplified to:

$$Z = \lambda \chi_1 \coth\left(\frac{l}{\lambda}\right) \quad (4)$$

with

$$\lambda = \sqrt{\frac{\zeta}{\chi_1}} \quad (5)$$

The observed impedance shape in Figs. 1 and 2 of a skewed semicircle can be obtained by making the reasonable assumptions

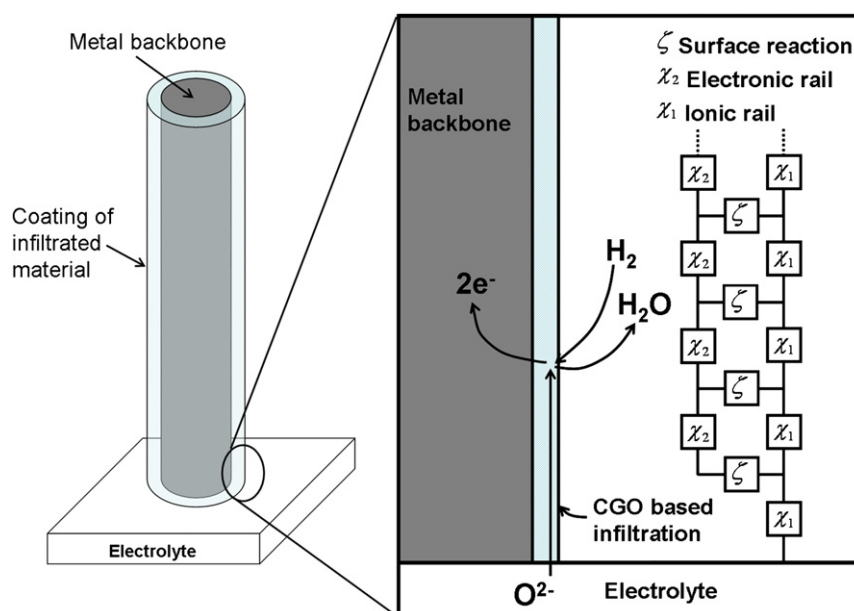


Fig. 3. Sketch of the situation where the anode microstructure is modeled as stainless steel columns coated with a CGO based infiltration. The electrochemical situation can be described by a transmission line.

of modeling the impedance of the ionic conduction as a resistance pr. unit length:

$$\chi_1 = r_{gi} \quad (6)$$

and the impedance of the electrochemical reaction ζ as a simple parallel combination between a resistor r_r and a constant phase element q_r (CPE):

$$\zeta = \frac{r_r}{1 + r_r q_r (j\omega)^{\alpha_r}} \quad (7)$$

Note that the resistor r_r represents the sum of the resistance associated with electron transport through the MIEC conducting CGO phase and the actual electrochemical reaction believed to take place at the surface of the infiltrated CGO based material. The total resistance of the ionic conduction R_{gi} , the electrochemical resistance R_r and the total CPE value Q_r associated with the porous electrode is given by the following relations:

$$R_{gi} = l \cdot r_{gi} \quad (8a)$$

$$R_r = \frac{r_r}{l} \quad (8b)$$

$$Q_r = q_r \cdot l \quad (8c)$$

Eq. (4) with the mentioned assumptions of Eq. (6) and Eq. (7) is in the following referred to as the Porous Electrode Theory (PET) model. In Figs. 1 and 2 good fits with the equivalent circuit $L(R_{HF} Q_{HF})PET(R_{conv}, C_{conv})$ can be seen, where L represents the inductance from wires etc. The thickness of the electrodes for the PET fitting has been estimated to be 46 μm from SEM images. For the spectrum with CGO infiltration at 650 $^{\circ}\text{C}$ in Fig. 1, the gas concentration impedance is neglectable and a good consistent fit for the PET impedance can be obtained. This is used as initial guess for the fitting of the impedance spectra with Ni:CGO infiltration in Fig. 2. The magnitude of the (R_{conv}, C_{conv}) gas concentration semicircle was estimated from complete fits with the $L(R_{HF} Q_{HF})PET(R_{conv}, C_{conv})$ equivalent circuit on the Ni:CGO infiltrated electrode in Fig. 2 and used in the fitting of the CGO infiltrated electrode in Fig. 1. The R_{conv} values under the given conditions ranged from 0.03 to 0.07 $\Omega \text{ cm}^2$ and is thus in accordance with previous findings [6]. The exponents α_{HF} and α_r for the CPE's Q_{HF} and q_r was kept constant in the fitting of the spectra in Figs. 1 and 2, respectively. The Arrhenius plots of the fitted r_{gi} and r_r values can be seen in Fig. 4. From these fitted values

it is possible to see that the addition of small amounts of Ni lowers the resistance associated with the surface reaction by a factor of 10 and decreases the activation energy considerably from 114 kJ mol^{-1} to 49 kJ mol^{-1} . It is also possible to see that the value and activation energy associated with ionic conduction within the porous electrode is slightly changed, with a change in activation energy from 89 kJ mol^{-1} to 129 kJ mol^{-1} , when Ni is added. The activation energy of 89 kJ mol^{-1} of the infiltrated CGO is a bit high compared to the reported activation energy of 45–50 kJ mol^{-1} for submicron sized CGO particles in Ref. [26]. A plausible explanation for this could be dissolution of Fe and/or Cr from the metal backbone into the CGO infiltrated particles during the elevated temperature of e.g. 800 $^{\circ}\text{C}$ in the impedance characterization procedure for the anodes. As an example, it is known that dissolution of manganese into oxide ion conducting YSZ affects the conductivity by e.g. an increase in the activation energy [27]. The TEM image in Fig. 5 shows a Ni:CGO infiltrated cermet anode, and it is possible to see that the Ni is distributed within the CGO matrix as nano sized particles. The presence of Ni in the CGO matrix and/or at the CGO grain boundaries may be the reason for the apparent increase in the activation energy in the ionic conductivity of the CGO matrix. A more detailed TEM characterization of the infiltrated Ni:CGO and the corrosion scale of the stainless steel based backbone will be reported in a later publication. From the fitted parameters with the PET model it is possible to calculate the characteristic electrochemical utilization thickness λ of the electrode, but also the PET DC resistance R_p as a function of electrode thickness l . The R_p as a function of electrode

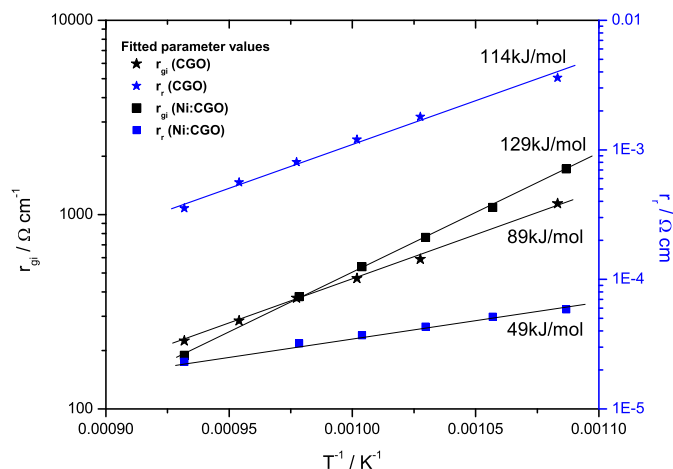


Fig. 4. Arrhenius plot of the fitted PET impedance model parameters r_{gi} and r_r for both the CGO and Ni:CGO infiltrated anodes presented in Figs. 1 and 2.

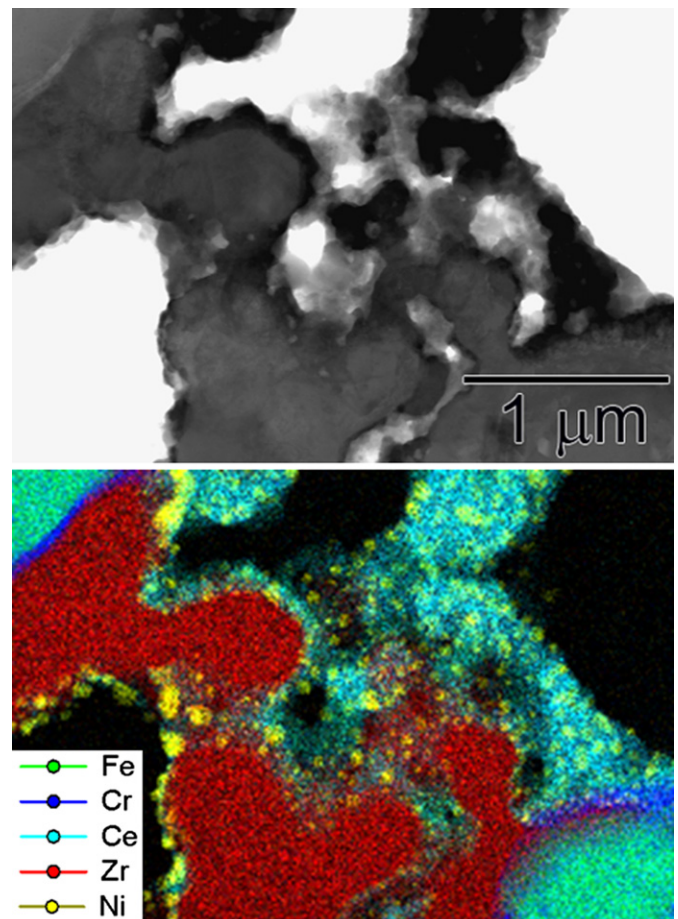


Fig. 5. TEM image of an infiltrated Ni:CGO MSC FeCr stainless steel and 3YSZ cermet anode.

thickness l at $T = 650^\circ\text{C}$ for both the CGO and Ni:CGO infiltrated anode is shown in Fig. 6A, while Fig. 6B shows the characteristic electrochemical utilization thickness λ as a function of temperature. From Fig. 6B it is possible to see a λ -value ranging from 17.8 to $12.6\ \mu\text{m}$ for the CGO infiltrated electrode and a λ -value ranging from 1.9 to $3.5\ \mu\text{m}$ for the Ni:CGO infiltrated electrode in the temperature range 650 – 800°C . Furthermore, it is possible to see the effect of the change in activation energy in the resistances r_{gi} and r_r shown in Fig. 4, when Ni is added. When the activation energy for r_r is larger than for r_{gi} , the characteristic utilization thickness λ decreases with increasing temperature. The change in activation energy with the presence of Ni results in the opposite situation with an increase in λ with increasing temperature.

As mentioned the HF impedance arc was in a previous study [6] described solely to be associated with grain boundaries within the high temperature sintered electrolyte. If this is the case, the arc is not expected to change significantly with time, operating parameters at temperatures 650 – 800°C and the actual preparation of the anode. However, it will become evident throughout the present study that the HF arc does change significantly with time, operating parameters, backbone composition and even on the amount of infiltrated material. Thus, the HF arc cannot be related to the electrolyte grain boundaries alone. The interpretation of the electrochemical response as a distributed impedance according to the

transmission line presented in Fig. 3 constrains the interpretation of the HF impedance arc to a process, which is connected in series with the PET response. For example, the HF arc cannot be an arc associated with electron transport through the formed protective chromium oxide scale between the stainless steel backbone and the CGO based infiltration. This would imply that the impedance ζ in Eq. (4) should be described by something else than the expression in Eq. (7) presenting a parallel coupling between a resistor and a CPE, which would lead to an impedance shape distinctively different from that observed. In other words the HF arc must be a process, which takes place before the coupling between the oxide ion conduction in the CGO phase χ_1 and the surface reaction ζ . Based on the magnitude of the capacitance it is possible to limit the possible assignments of the phenomenon and thereby the regions in the symmetrical cell, which is likely to be involved in the response [28]. For comparison of CPE element values an equivalent capacitance C_W can be calculated [29]:

$$C_W = (R^{1-\alpha}Q)^{1/\alpha} \quad (9)$$

The C_W values of the HF arc were $6.04 \times 10^{-7}\ \text{F cm}^{-2}$ and $5.13 \times 10^{-7}\ \text{F cm}^{-2}$ for the spectra with CGO and Ni:CGO infiltration in Figs. 1 and 2, respectively. The α values ranged from 0.73 to 0.77. These C_W values suggest that the HF capacitance could potentially be associated with a process at the electrode/electrolyte interface [28].

3.2. Effect of the amount of infiltrated material

In Fig. 7 a comparison is seen between a normal Ni:CGO infiltrated anode and one which has been infiltrated with 33% less amount of Ni:CGO. It is clearly seen that both the HF arc and the intermediate frequency PET response increases when smaller amounts of Ni:CGO is infiltrated. The increase in the intermediate frequency arc is expected, but the increase in the HF arc indicates strongly that the arc is not solely associated with the grain boundaries within the approximately $120\ \mu\text{m}$ thick ScYSZ electrolyte. There is apparently a clear effect of the amount of infiltration and the magnitude of the HF arc and since the arc must be in series with the PET response as mentioned in section 3.1 a possible explanation for the origin of the arc could be that the arc is associated with oxide ion charge transfer from the oxide ion conducting CGO rail in the PET model to the ScYSZ electrolyte, that is, an oxide ion charge transfer between the anode and the ScYSZ electrolyte. If such a charge transfer resistance exists it is expected to be sensitive

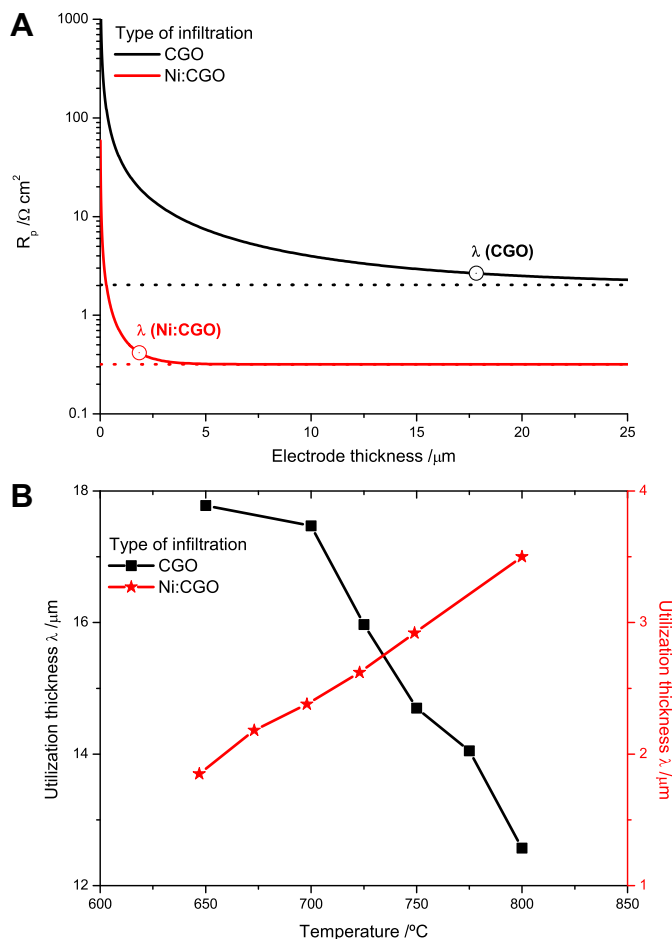


Fig. 6. Based on the PET impedance model fits in Figs. 1 and 2 the following calculations have been made A) The PET impedance model polarization resistance R_p as a function of electrode thickness l for both the CGO infiltrated anode in Fig. 1 and the Ni:CGO infiltrated anode in Fig. 2 at 650°C . B) The characteristic electrochemical utilization thickness λ as a function of temperature for both the CGO and Ni:CGO infiltrated symmetrical cells in Figs. 1 and 2.

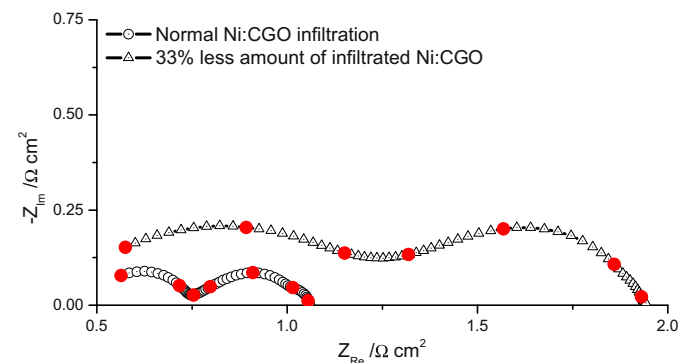


Fig. 7. Comparison between a normal infiltrated symmetrical cell with MSC cermet anodes and a cell with 33 wt% less Ni:CGO infiltration at 650°C in a 3% humidified hydrogen atmosphere. The red dots ● denote each frequency decade in the frequency range 1 MHz–1 Hz. (For interpretation of the references to color in this figure legend, the reader is referred to the web version of this article.)

towards changes in the amount of CGO at the anode/electrolyte interface. It would also be sensitive to changes in the CGO microstructure, e.g. sintering (grain growth and necking) of the CGO based infiltration during the initial startup step (at a temperature above the operation temperature of 650 °C). Such a charge transfer would also be expected to couple with the double layer capacitance of the anode/electrolyte interface, which is in accordance with the HF capacitance interpretation discussed at the end of section 3.1.

3.3. Effect of composition of the backbone

An increase in the content of FeCr in the cermet backbone resulted in a denser microstructure as can be seen from the SEM images in Fig. 8. The backbone with a higher FeCr content was infiltrated with Ni:CGO according to the procedure described in section 2.1. Comparing the impedance of the cermet anodes with normal (50 vol.%) FeCr content and 40% increased FeCr content in Fig. 9, it is first of all possible to see that the total resistance $R_s + R_p$ of the anode with a higher FeCr content is smaller than for the normal cermet composition. Furthermore, it is also possible to see that both the HF and the intermediate frequency PET response are smaller for the anode with increased FeCr content. This illustrates the assumption already made that the presence of the 3YSZ phase does not contribute significantly to the electrochemistry of the anode. It primarily seems to act as a processing agent in the anode backbone preparation. In order to extend the active area from the very anode/electrolyte interface and obtain a distributed network as presented in Fig. 3 it is necessary to either have an electronic conducting backbone coated by infiltration with an ionic conducting material (PET type I) or an ionic conducting backbone coated by infiltration with an electronic conducting material (PET type II). In the present case with the FeCr and 3YSZ cermet the FeCr acts an electronic conducting backbone, while the 3YSZ acts as an ionic conducting backbone. The CGO in the Ni:CGO infiltration is under the very reducing condition of a humidified hydrogen atmosphere a MIEC conductor. Thus, the response from both the PET type I and the PET type II transmission lines come in principle into play in the present case. However, since the impedance of the surface reaction ζ is the same for both types of transmission lines, the dominating one, will be the one with the best combination of ionic and electronic conduction according to Eqs. (2) and (3). Since the electronic conduction of the FeCr metal is superior compared to that of CGO and the fact that CGO is a fairly good ionic conductor and comparable to 3YSZ, it is not a big surprise, that the data of Fig. 9 suggest the anode performance to be determined by the impedance of the distributed mechanism depicted to the left in Fig. 3 (PET type I transmission line).

3.4. Effect of preconditioning during initial startup

Prior to any type of testing, the infiltrated cermet anodes have only experienced a temperature of 350 °C. Thus, upon startup and thereby ramping of the temperature to 650 °C a growth of the crystallites of the infiltrated CGO and hence change in the impedance of the anode is expected. Fig. 10A shows the initial development of the total resistance ($R_s + R_p$) of a representative symmetrical cell as a function of time in a 3% humidified hydrogen atmosphere after the cell had reached a temperature of 650 °C. From Fig. 10A it is possible to see that it is necessary with two characteristic time constants τ to describe the initial transient like behavior during startup. Each term with an exponential function in the fitting equation represents a first order performance decay process with a characteristic time constant τ . The anode performance decay consists of a fast process with $\tau_1 \sim 5$ h and a slow process with $\tau_2 \sim 52$ h. From the ADIS in Fig. 10B of the spectra during the startup two peaks at ~ 30 Hz and ~ 300 kHz can be seen, respectively. These peaks correspond to the intermediate frequency PET arc and the HF arc described in the beginning of section 3.1. The ADIS plot shows that the changes in the intermediate frequency 30 Hz PET peak levels off relatively fast, in contrast to the high frequency peak, which changes during the whole measurement period. The development of the two ADIS peaks corresponds well with the characteristic time constants τ found from the fitting in Fig. 10A. The characteristic time constant $\tau_1 \sim 5$ h of the intermediate frequency 30 Hz PET arc is in excellent agreement with the characteristic time constant for the CGO self limiting crystallite grain growth reported in Ref. [30]. Thus, the increase of the PET arc could very well be due to CGO grain growth and hence decrease in the surface area, which makes sense in the given context. The characteristic time constant $\tau_2 \sim 52$ h of the changes in the HF arc may be interpreted, as mentioned in section 3.2, as a change in the resistance of the oxide ion transfer process between the anode and the electrolyte.

3.5. Robustness of infiltration towards temperature

For electrodes based on infiltration of submicron sized particles a key issue is the tendency of the submicron particles to agglomerate and/or sinter with the result of grain growth and thereby a loss of active surface area and possible “nano effect”. Stabilization of the submicron particles are therefore of paramount importance for the long term durability. The durability of the anode during operation at 650 °C has already been demonstrated in the galvanostatic long term tests reported in Ref. [4]. However, as mentioned in the introduction, an in-situ sintering step of the cathode is

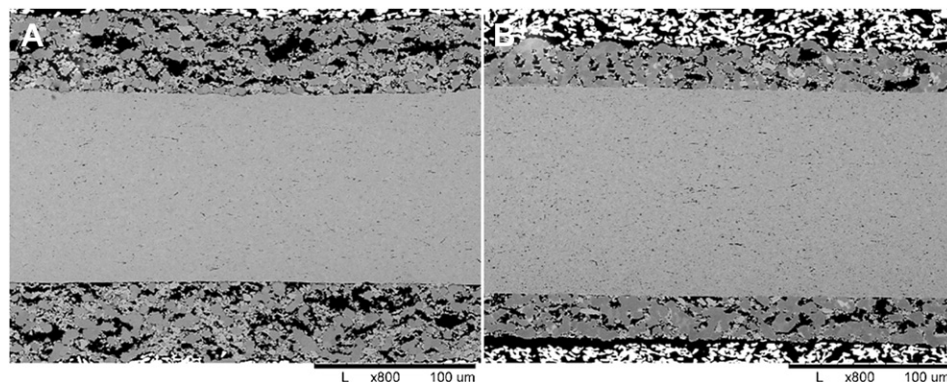


Fig. 8. Overview micro structural SEM images of symmetrical cells with MSC anodes. The bright layer on top of the symmetrical cells is the applied Pt paste current collecting layer. A) Symmetrical cell with normal MSC anodes B) Symmetrical cell with MSC anodes with 33% more stainless steel than normally.

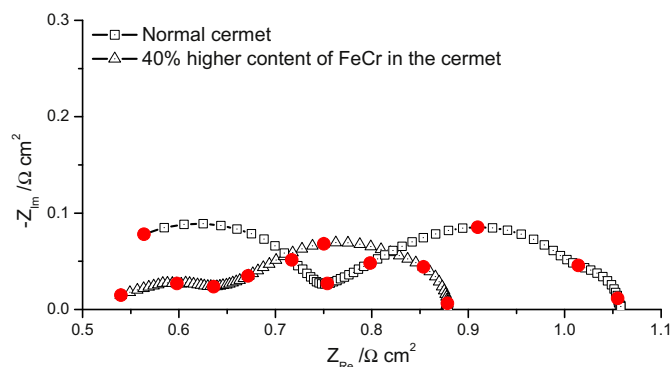


Fig. 9. Comparison between the impedance of an infiltrated normal cermet backbone and an infiltrated cermet backbone with 33% more stainless steel. The measurements are at 650 °C in a 3% humidified hydrogen atmosphere. The microstructure of the symmetrical cells is shown in Fig. 8. The red dots ● denote each frequency decade in the frequency range 1 MHz–1 Hz. (For interpretation of the references to color in this figure legend, the reader is referred to the web version of this article.)

necessary during startup of the cell. The question is therefore, what impact this heat treatment step at elevated temperatures has on the performance and durability of the infiltrated Ni:CGO anode. In order to shed light on this aspect the test presented in Fig. 11A and B

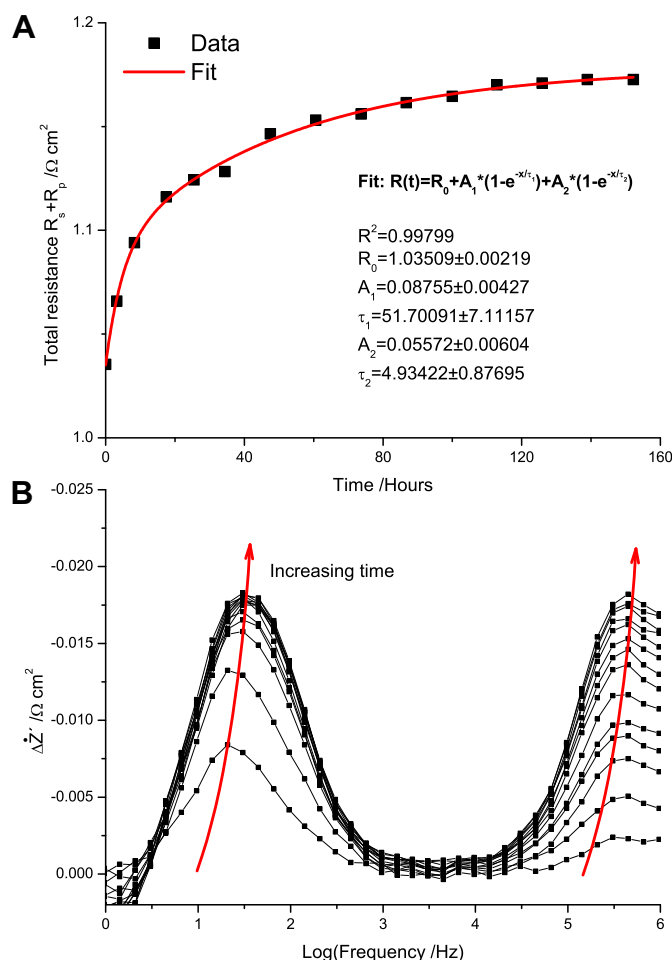


Fig. 10. A) Development in the total resistance $R_t = R_s + R_p$ immediately after the symmetrical cell has been heated up from room temperature to 650 °C and the atmosphere has been switched from 9% H_2 in N_2 to 3% humidified hydrogen. The R_t development is fitted with a biexponential expression, where each term containing an exponential function represents a first order decay process with a characteristic time constant τ . B) ADIS of the impedance during the R_t development shown in A).

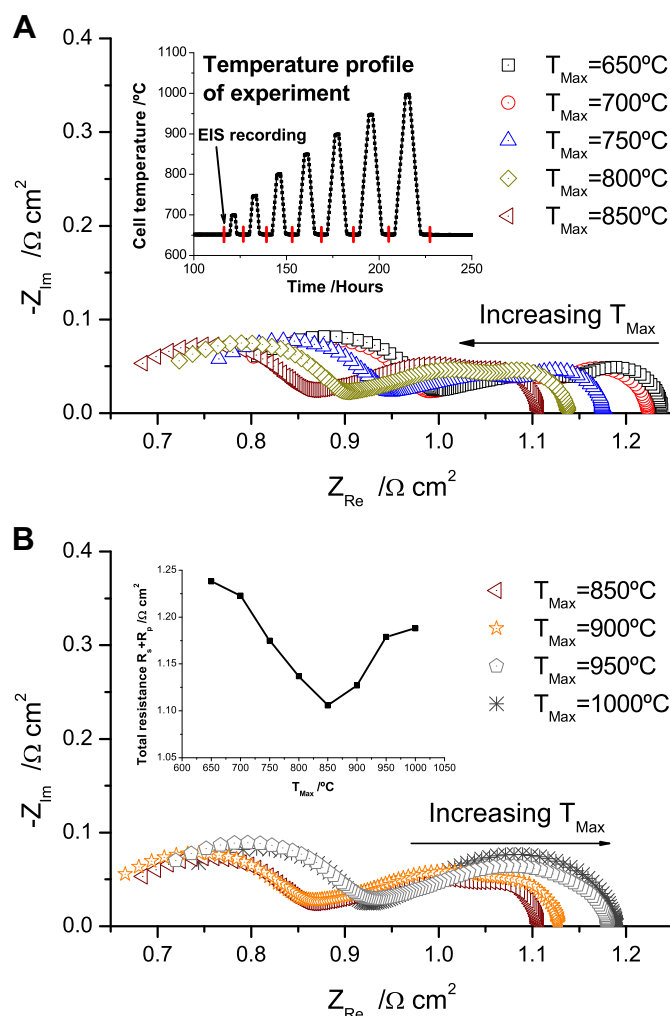


Fig. 11. A) + B) Development of the impedance in 3% humidified hydrogen at 650 °C after the symmetrical cell with MSC anodes has experienced increasing T_{max} temperatures in steps of 50 °C from 650 °C to 1000 °C. During the elevated temperatures above 650 °C the atmosphere was dry hydrogen. Prior to the temperature profile shown in the inset figure of A) The cells had been preconditioned at 650 °C until the impedance did not change significantly with time as in Fig. 10.

was performed. After a conditioning period at 650 °C where the impedance in 3% humidified hydrogen no longer changed significantly with time, the cell was subjected to 2 h temperature treatment periods with an increasing T_{max} temperature according to the temperature profile shown in the inset of Fig. 11A. During the temperature ramping and the 2 h dwell time at increased T_{max} temperature dry hydrogen was fed to the cells. This was done in an attempt to only observe the effect of CGO sintering by minimizing possible effects from corrosion of the stainless steel based backbone. At 650 °C where an impedance spectrum was recorded after each segment with increased T_{max} the cells were supplied with 3% humidified hydrogen. From the results of Fig. 11A and B it is possible to see that the performance of the Ni:CGO infiltration is surprisingly robust towards higher temperatures. It is surprising since any further sintering or agglomeration of the infiltrated submicron particles is expected to decrease the active surface area and thus the performance. On the contrary, the effect of an increasing T_{max} actually results in an reduced total resistance $R_s + R_p$ of the anode up to $T_{max} = 850$ °C after which the expected increase in total resistance with an increasing T_{max} temperature is seen. Nonetheless, the performance after a $T_{max} = 1000$ °C is still better than after

the initial $T_{\max} = 650$ °C. The result is rather surprising, but may partly be understood in terms of the self limiting CGO grain growth at temperatures up to 1100 °C reported in Ref. [30] and the TEM image of the Ni:CGO infiltrated metal based backbone in Fig. 5. The TEM image illustrates how the added Ni is trapped as small 10–50 nm sized Ni particles within the CGO matrix, which probably prevents the Ni particles from further growth. A closer inspection of the acquired impedance spectra in Fig. 11A and B revealed that the intermediate frequency PET impedance contribution actually increased slightly after each increment in T_{\max} . The origin to the observed minimum in the total resistance ($R_s + R_p$) after $T_{\max} = 850$ °C is due to an even greater decrease in R_s and the HF impedance arc than the increase in the intermediate frequency PET impedance contribution. These observations may be interpreted in the following way: The unavoidable (though to some degree restricted) grain growth of the infiltrated phase with increasing T_{\max} will result in a decrease in the active surface area, which explains the increase in the resistance associated with the PET impedance response after each increment in the T_{\max} temperature. The increase in T_{\max} and thus the sintering of the infiltrated materials may on the other hand also have a beneficial effect such as a better contact between the interface of the CGO ionic rail in the PET anode response and the ScYSZ electrolyte. This oxide ion charge transfer between the ScYSZ electrolyte and the anode is believed to be related with the HF arc and a change in contact between these two parts would explain the observed changes. As the infiltrated phase sinters and the particles increase in size a better contact is expected until a certain critical point. Initially, the infiltrated material covers the metal based backbone as a thin film, but when at some point the particles reach a certain size, the infiltration distribution change from a film into a more island or mesh like distribution. This type of mechanism may explain the observed changes with increasing T_{\max} in the serial resistance R_s , the HF arc and the PET intermediate frequency arc. The results of Fig. 11A and B have been reproduced several times.

3.6. Effect of water vapour and corrosion of the metal based backbone

So far the effect of high steam content in the fuel has not been addressed on the type of anode in the present study. It is important since in the end, the MSC's need to be able to withstand the technological relevant condition of high fuel utilization without detrimental corrosion. Previous studies on symmetrical cells have not exceeded a degree of hydrogen humidification above 3% [6] and in single cell testing the cells have been operating with low FU < 10% [3,4,6]. Fig. 12 shows ADIS of a stepwise increase in the water content in the gas composition at 650 °C, where the initial spectrum with the gas composition 3% H₂O/97% H₂ is used as the reference spectrum. The dwell time at each degree of humidification was 7.5 h. Prior to the stepwise increase in the H₂O gas molar fraction the cells went through a preconditioning as shown in Fig. 10. From the ADIS in Fig. 12 it is possible to see a clear relatively large reduction in the impedance around 2 Hz and 20 Hz when the gas H₂O molar fraction is increased from 3% to 20%. These two changes are ascribed to a lowering of the resistance associated with gas conversion located at ~2 Hz and the gas diffusion at ~20 Hz and are in well accordance with similar gas shifts for the traditional Ni/YSZ cermet SOFC anodes [18]. The gas conversion resistance changes dramatically in the two extremes of either low H₂O or low H₂ molar fractions [15]. On further increase of the gas H₂O molar fraction from 20% to 86% no further significant change in the gas diffusion and gas conversion is seen. For the traditional Ni/YSZ cermet SOFC anodes such gas shifts usually also improves the impedance arc associated with the electrochemistry. However,

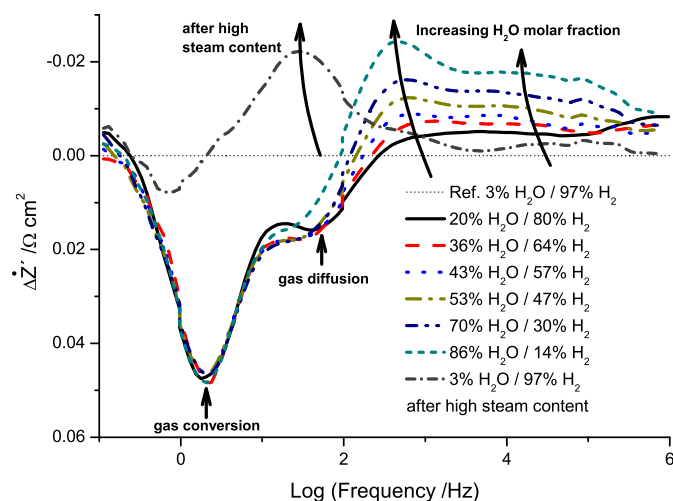


Fig. 12. ADIS of a cell at 650 °C where the H₂O molar fraction in the two component H₂O/H₂ atmosphere has been increased stepwise from 3% to 86%. The cell was prior to the increase in H₂O molar fraction preconditioned at 650 °C in 3% hydrogen until no further significant change with time could be detected with impedance spectroscopy at OCV as shown in Fig. 10.

the opposite is seen in the present case of the infiltrated MSC anode. From the ADIS in Fig. 12 it is possible to see an increase in the impedance above 100 Hz after the gas shift from 3% to 20% humidified hydrogen. On further increase of the humidification this increase in resistance becomes even more evident with a clear peak around 300 Hz. However, ADIS of the spectrum in 3% humidified hydrogen after the sequence with high molar fractions of water 20–86% show the predominant change to have taken place around 30 Hz, which is in accordance with the PET impedance response in Fig. 10. Using the 20% humidified hydrogen impedance spectrum as reference for the ADIS of the spectra with 20–86% humidified hydrogen removes the gas diffusion and gas conversion ADIS peaks in Fig. 12 and confirms that the change during 20–86% humidification is located around 300 Hz. Furthermore, visual inspection of the spectra also confirms that the predominant change during high degrees of humidification is the PET impedance response. Thus, the presence of high molar water fractions seems to shift the PET response towards a higher frequency. In this respect it may be worthwhile to remember that the conductivity of the MIEC CGO depends on the oxygen partial pressure and thus the degree of humidification [31]. A change in the electronic and the ionic conductivity will affect the PET model parameters r_r and r_{gi} . It is probably not the complete explanation for the observed change in frequency of the PET response, but at least an important aspect. The thermal prehistory probably also has a role. In previous studies on this type of anodes, where the cells had experienced a temperature of 750 °C prior to measurements at 650 °C, the PET impedance response was shown to be located in the region of a few hundred hertz [6]. ADIS of the spectra for the similar case in Fig. 2 also shows the PET response to be located in the region of a few hundred hertz. Thus, the thermal prehistory and maybe also the prehistory with respect to the experienced humidified fuel atmosphere seem to affect the PET response and hence the associated characteristic frequency. The clear observed degradation in Fig. 12 with the presence of a high H₂O molar fraction shows at least that water has an impact on the anodes of the present study. A natural consequence of higher steam contents would be changes in the protective chromium oxide scale of the FeCr stainless steel. This would change the interface between the infiltrated Ni:CGO layer and the stainless steel based backbone and a thicker chromium oxide scale and/or

change in its composition would most likely affect the electron transport to the electrochemical active gas/solid interface of the Ni:CGO infiltration. The consequence would be changes of r_r and q_r in the PET impedance model and thus the observed change. To further understand the impact of corrosion on the impedance the following accelerated test was conducted subsequent to the gas variations in Fig. 12. The cell was heated up to 750 °C and an 80% H₂O/20% H₂ atmosphere was supplied to the cells. Under these very harsh conditions the stainless steel based backbone is expected to corrode relatively fast. Periodic impedance recording showed the degradation depicted in Fig. 13A. The further grain growth of the CGO as the temperature was increased from 650 °C to 750 °C was, as discussed in section 3.4, expected to level of with a characteristic time constant around 5 h according to Ref. [30] and the interpretation discussed in section 3.4. Thus, the observed ongoing degradation for 150 h must contain a contribution from the corroding stainless steel based backbone. As can be seen from the ADIS in Fig. 13B the main degradation occurs around 200 Hz where the PET response is located. However, a smaller change

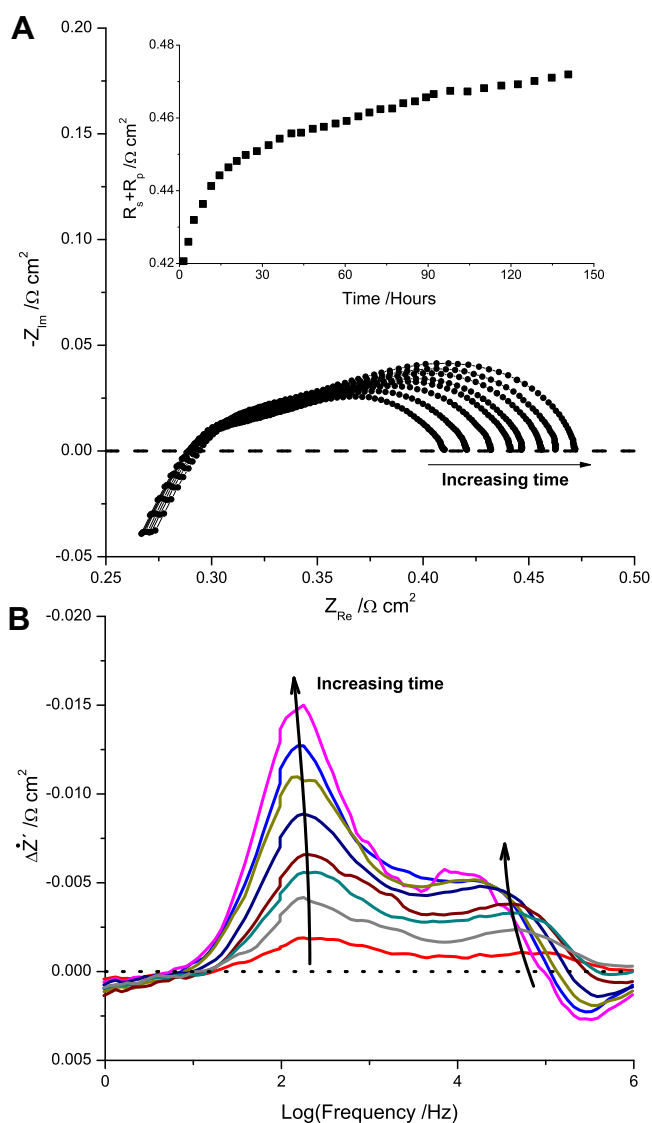


Fig. 13. A) Impedance development at 750 °C after the cell has been ramped from 650 °C to 750 °C and the supplied gas has been at 750 °C switched from 3% to a 80% humidified hydrogen atmosphere. B) ADIS of the impedance spectra in A).

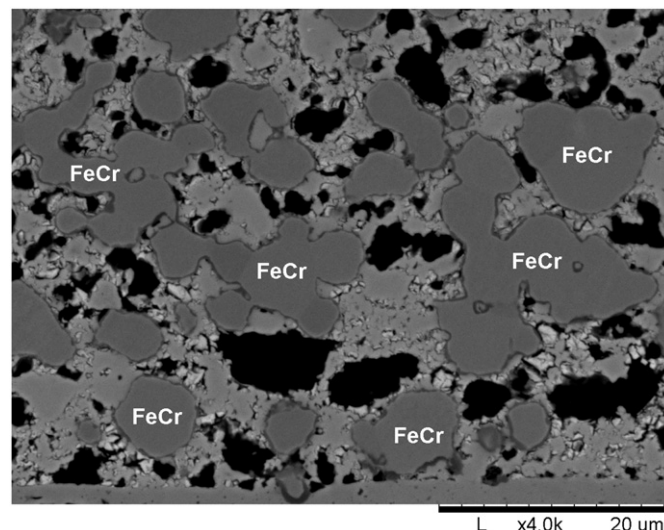


Fig. 14. SEM (back scatter mode) micrograph of the active anode layer after the test in Fig. 13 in an 80% H₂O/20% H₂ atmosphere at 750 °C. FeCr illustrates some of the metal particles in the cermet layer. The dark grey rim/areas around the FeCr particles are where the FeCr particles have experienced corrosion during the test. The light grey particles in the cermet layer correspond to the YSZ phase. The infiltrated material (Ni:CGO) is visible as the bright areas covering all surfaces exposed to the fuel gas in the cermet layer.

around 100 kHz is also clear. This suggests that high molar fractions of water also have an impact on the interface between the CGO particles and the ScYSZ electrolyte and maybe on the sintering of CGO particles, which makes analysis of the various resistance contributions by variations in the gas composition relatively complicated. It is unclear at this stage what happens to the Fe when the FeCr stainless steel corrodes and the protective chromium oxide scale is formed and what effect water can have on the mobility of the various elements. The anode in the present study is a relatively complicated system. The results of section 3.5 showed that the infiltrated Ni:CGO catalyst seems to be very tolerant towards further sintering. Thus, the results indicate that the presence of water affects the Ni:CGO infiltration, the stainless steel based backbone and the interaction between these phases. A postmortem SEM image of the anode from the test in Fig. 13 is shown in Fig. 14, which reveal that the stainless steel particles is covered with a clear observable dark rim, which is identified as the formed chromium rich protective oxide scale. Thus, some corrosion has taken place, which at least is partly observed as the change in impedance around 200 Hz in Fig. 13. At the stage where the molar fraction of chromium in the stainless steel bulk reaches a certain lower threshold level around 15%, iron oxides starts to form and breakaway corrosion will occur and as a result complete failure of the MSC [32,33]. The smaller particles in the cermet anode layer compared to the metal support has due to their size a smaller reservoir of chromium, which means, that these will be the first to experience the detrimental break away corrosion with formation of iron oxides.

4. Conclusions

The detailed impedance spectroscopy study provided valuable insight into the various processes of the Ni:CGO infiltrated novel cermet anode for MSC's. It was shown that the intermediate frequency arc of the 3 clearly resolved impedance arcs cannot be described as a simple suppressed semicircle. Instead, it was shown that porous electrode theory (PET) represented as a transmission

line response can account for the impedance arc. The PET model allowed extraction of parameters representing physical processes within the porous electrode and thereby a more detailed insight into the effect of adding minor amounts of Ni into the infiltrated CGO. Further, it is also possible from the fitted parameters to calculate important characteristics such the PET polarization resistance as a function of the electrode thickness and the electrochemical utilization thickness λ as a function of temperature.

The studies also revealed that the observed high frequency impedance arc cannot solely be a consequence of the grain boundaries within the electrolyte as previously assumed, since it was shown to be dependent on the amount of infiltration, backbone microstructure and the anode prehistory. Instead, the results pointed towards an oxide ion charge transfer resistance between the electrolyte and the infiltrated anode. The measurements indicated furthermore the presence of 3YSZ to be electrochemically of minor importance.

The robustness of the infiltration towards sintering and/or agglomeration at elevated temperature was also studied. The results showed that the performance of the infiltrated submicron sized particles was surprisingly robust. Instead of a poorer performance a slight increase in the performance was observed after treatment at increased T_{\max} temperatures. TEM analysis revealed the submicron sized Ni particles to be trapped within the CGO matrix, which along the self limiting grain growth of the CGO apparently is able to stabilize the submicron structured anode. In the light of these observations the long term durability is therefore most likely limited by the corrosion tolerance of the FeCr stainless steel and thus the cermet anode layer, which contains the smallest FeCr metal particles.

Acknowledgement

This work was supported financially by Topsoe Fuel Cell A/S, the EU project FP7-211940 (METSOFC), and The Danish National Advanced Technology Foundation. Karin Brodersen and Dr. Åsa H. Persson at DTU Energy Conversion are acknowledged for helpful contribution in the fabrication of the samples used in this work, while Dr. Hsiang-Jen Wang is greatly acknowledged for help with respect to the TEM analysis.

References

- [1] M.C. Tucker, G.Y. Lau, C.P. Jacobson, L.C. DeJonghe, S.J. Visco, J. Power Sources 171 (2007) 477–482.
- [2] M.C. Tucker, J. Power Sources 195 (2010) 4570–4582.
- [3] P. Blennow, J. Hjelm, T. Klemensø, S. Ramousse, A. Kromp, A. Leonide, A. Weber, J. Power Sources 196 (2011) 7117.
- [4] T. Klemensø, J. Nielsen, P. Blennow, Å.H. Persson, T. Stegk, B.H. Christensen, S. Sønderby, J. Power Sources 196 (2011) 9459.
- [5] M. Brandner, M. Bram, J. Froitzheim, H.P. Buchkremer, D. Stoeber, Solid State Ionics 179 (2008) 1501–1504.
- [6] P. Blennow, J. Hjelm, T. Klemensø, Å.H. Persson, S. Ramousse, M. Mogensen, Fuel Cells 11 (2011) 661.
- [7] Zhangbo Liu, Beibei Liu, Dong Ding, Zhiyi Jiang, Changrong Xia, Int. J. Hydrogen Energy, <http://dx.doi.org/10.1016/j.ijhydene.2011.11.115>.
- [8] P. Blennow, M. Mogensen, EP2031675(A1), 2009.
- [9] T. Ramos, K. Thydén, M. Mogensen, ECS Trans. 28 (2010) 123.
- [10] S.H. Jensen, A. Hauch, P.V. Hendriksen, M. Mogensen, N. Bonanos, T. Jacobsen, J. Electrochem. Soc. 154 (12) (2007) B1325.
- [11] S.H. Jensen, J. Hjelm, A. Hagen, M. Mogensen, Handbook of Fuel Cells: Advances in Electrocatalysis, Materials, Diagnostics and Durability, vols. 5 & 6, Wiley, 2009 (Chapter 53).
- [12] B.A. Boukamp, Solid State Ionics 20 (1986) 31.
- [13] W.G. Bessler, in: Proceedings of the 7th European Solid Oxide Fuel Cell Forum, Lucerne, Switzerland, 2006, p. P0707.
- [14] W.G. Bessler, S. Geweis, J. Electrochem. Soc. 154 (2007) B548.
- [15] W.G. Bessler, S. Geweis, J. Electrochem. Soc. 153 (2006) A1492.
- [16] T. Jacobsen, P.V. Hendriksen, S. Koch, Electrochim. Acta 53 (2008) 7500.
- [17] S. Primdahl, M. Mogensen, J. Electrochem. Soc. 145 (1998) 2431.
- [18] R. Barfod, M. Mogensen, T. Klemensø, A. Hagen, Y.L. Liu, P.V. Hendriksen, J. Electrochem. Soc. 154 (2007) B371.
- [19] R. de Levie, P. Delahay, in: Advances in Electrochemistry and Electrochemical Engineering, vol. 6, 1967, p. 329.
- [20] A. Lasia, M. Schlesinger (Eds.), Modern Aspects of Electrochemistry, vol. 43, Springer, 2009, p. 67.
- [21] V. Sonn, A. Leonide, E. Ivers-Tiffée, J. Electrochem. Soc. 155 (2008) B675.
- [22] J. Nielsen, T. Jacobsen, M. Wandel, Electrochim. Acta 56 (2011) 7963.
- [23] S.B. Adler, J.A. Lane, B.C. Steele, J. Electrochem. Soc. 143 (111) (1996) 3554.
- [24] J. Bisquert, G. Garcia-Belmonte, F. Fabregat-Santiago, A. Compte, Electrochem. Commun. 1 (1999) 429.
- [25] J. Bisquert, G. Garcia-Belmonte, F. Fabregat-Santiago, N.S. Ferriols, P. Bogdanoff, E.C. Pereira, J. Phys. Chem. B 104 (2000) 2287.
- [26] T. Mori, R. Buchanan, D.R. Ou, F. Ye, T. Kobayashi, Je-Deok Kim, J. Zou, J. Drennan, J. Solid State Electrochem. 12 (2008) 841.
- [27] T. Kawada, N. Sakai, H. Yokokawa, M. Dokiya, Solid State Ionics 50 (1992) 189.
- [28] J.T.S. Irvine, D.V. Sinclair, A.R. West, Adv. Mater. 2 (1990) 132.
- [29] T. Jacobsen, B. Zachau-Christiansen, L. Bay, S. Skaarup, in: Proceedings of the 17th Risø International Symposium on Materials Science: High Temperature Electrochemistry: Ceramics and Metals, 1996, p. 29.
- [30] J.L.M. Rupp, A. Infortuna, L.J. Gauckler, Acta Mater. 54 (2006) 1721.
- [31] H.J. Park, G.M. Choi, J. Eur. Ceram. Soc. 24 (2004) 1313.
- [32] H.E. Evans, A.T. Donaldson, T.C. Gilmour, Oxid. Met. 52 (1999) 379.
- [33] G.Y. Lai, ASM Int. (2007).